RESEARCH ARTICLE | SEPTEMBER 16 2024

Layered heterogeneous structures integrated device for multiplication, division arithmetic unit and multiple-physical sensing ⊘

Jie Xu (徐杰) ⓘ ; Ming-Zhe Zhang (张明哲) ⓘ ; Zhao Tang (唐钊); Hai-Feng Zhang (章海锋) ✉ ⓘ

Check for updates

View Online

Export Citation
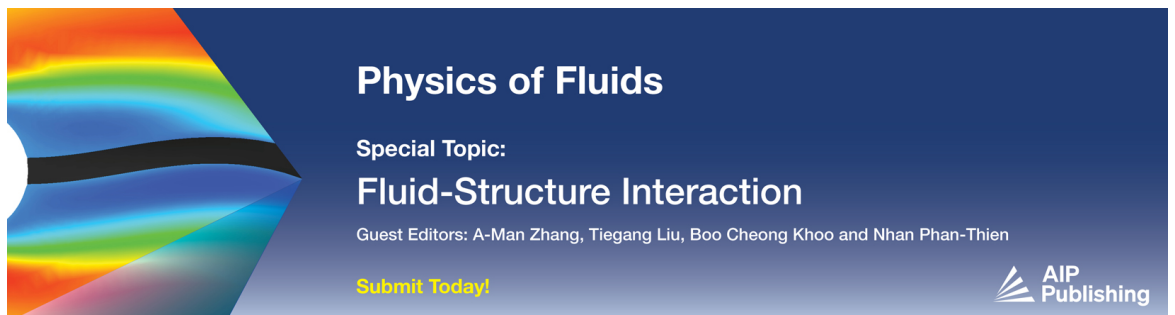
Physics of Fluids

Special Topic:

Fluid-Structure Interaction

Guest Editors: A-Man Zhang, Tiegang Liu, Boo Cheong Khoo and Nhan Phan-Thien

Submit Today!

AIP Publishing

AIP Publishing

Layered heterogeneous structures integrated device for multiplication, division arithmetic unit and multiple-physical sensing

View Online   Export Citation   CrossMark

Jie Xu (徐杰), Ming-Zhe Zhang (张明哲), Zhao Tang (唐钊), and Hai-Feng Zhang (章海锋)[a]

AFFILIATIONS

College of Electronic and Optical Engineering and College of Flexible Electronics (Future Technology), Nanjing University of Posts and Telecommunications, Nanjing 210023, China

[a]Author to whom correspondence should be addressed: hanlor@163.com and hanlor@njupt.edu.cn

ABSTRACT

A layered heterogeneous structure (LHS), consisting of silver, liquid crystal, and nonlinear dielectric layers, is proposed to realize functions of computing and sensing. By leveraging the optical Tamm state, the intrinsic absorption principle of liquid crystal, and nonlinear effects, the design of an integrated device capable of passive multiplication and division operations, along with high-performance multi-physical quantity sensing functionalities, is achieved. The given LHS exhibits Janus properties, with different physical functions manifested depending on the direction of electromagnetic wave (EW) propagation. During forward propagation of EWs, the LHS displays high and sharp absorptivity peaks at 774.8 and 1517.6 nm. The relationship between the two peaks approximates a frequency multiplication factor of 1.960, enabling signal multiplication. Furthermore, the two absorptivity peaks at different wavelengths facilitate the sensing of serum creatinine solution concentration and external pressure, with sensitivity (S), quality factors (Q), and figure of merit (FOM) of 266.76 μmol L^{-1}/nm and 213.33 GPa/nm, as well as 248.76 and 348.22, 84.1 L $(\mu$mol$)^{-1}$ and 49.06 GPa^{-1}, respectively. During backward propagation of EWs, absorptivity peaks with distinct resolutions are observed at 1423 and 2809 nm, with a multiple relationship between them of 1.974, enabling frequency doubling for signal division. Additionally, the absorptivity curve facilitates temperature sensing over a wide range from 257 to 347 K. Owing to the unique temperature S of liquid crystal, different sensitivities and resolutions are observed at 257 to 297 K and 307 to 347 K, with S of 1.015 and 0.686 K/nm, and corresponding Q and FOM of 21.57 and 12.576, 0.076 K^{-1} and 0.003 04 K^{-1}, respectively.

I. INTRODUCTION

The layered heterogeneous structure (LHS) refers to a material with a periodic structure in the one-dimensional direction, which can be regulated and managed through the strategic arrangement of the dielectric constant.[1,2] Due to its unique electromagnetic properties, the prohibition of electromagnetic wave (EW) propagation within a specific frequency range can be easily achieved by Bragg diffraction, forming a photonic bandgap.[3,4] The existence of this bandgap makes LHS widely used in optical filters, sensors, and encoders.[5–7] The optical sensor, benefiting from its high sensitivity (S) and fast response time, is suitable for passive and high-quality requirements in practical applications.[8,9] Due to the advantages of miniaturization and integration, and the presence of the photonic bandgap, LHS is extensively utilized in the design of optical sensors, particularly optical cavity sensors.[10] In 2022, Zaky *et al.* proposed a highly sensitive remote temperature sensor based on Tamm resonance using a one-dimensional photonic crystal structure, optimized for high sensitivity and signal-to-noise ratio through the coupling of porous silicon properties and Tamm resonance.[11] In 2022, Khani and Hayati introduced a novel optical biosensor configuration for cancer cell detection, featuring one-dimensional photonic crystal lattices coupled with metal–insulator–metal plasmonic waveguides.[12] These studies focused solely on the detection of a single physical quantity and exhibited sensing characteristics only during single-directional EW transmission through the LHS.

With the advancements in science and technology and the goal of cost reduction, this paper integrates the optical Tamm state, the intrinsic absorption principle of liquid crystal (LC) which offers nearly constant absorptivity characteristics from the visible band to the infrared region, and the nonlinear effect with the LHS to form high and sharp absorptivity peaks, enabling the detection of multiple physical quantities.[13–15] Additionally, the Janus properties, inspired by the two-faced

god Janus in Roman mythology, symbolize the unity of opposites and transformations which also describes materials or systems that exhibit two distinct physical or chemical properties on the same structure.[16]

In recent years, optical frequency converters have been widely used to adapt the frequency of light waves to different application requirements.[17] This conversion is typically achieved through nonlinear optical effects, such as second harmonic generation or difference frequency generation.[18] In these processes, when light passes through a nonlinear medium, the frequency of the input EW is converted into a new frequency due to the nonlinear response of the medium. In 2011, Rivoire et al.[19] described a photonic crystals nanocavity with multiple spatially overlapping resonances, which can serve as a platform for nonlinear frequency conversion with resonance intervals up to 523 nm. When the frequency conversion interval is exactly one time, the frequency doubling phenomenon is generated to be used in the design of 2-bit signal encoders and multiplication and division operators.[20] For instance, this has potential applications in optical neural networks, high-speed data processing, and complex pattern recognition.[21] By exploiting the speed of light and the parallel processing power of light, ultra-high-speed and highly efficient data processing can be achieved. In 2023, Qu et al. proposed[22] a vertical photonic cavity embedded with a nonlinear material in a photonic crystal to achieve resonance enhancement of the second harmonic, opening new possibilities for small laser frequency converters that could revolutionize the fields of nonlinear optics and photonics. However, because nonlinear optics cannot achieve precise control, the generation of second harmonic and difference frequency often appears at a lower frequency, which is not robust in practical applications. Therefore, a broader application scenario is involved in directly generating peaks of different frequencies without relying on the processes of second harmonic and difference frequency generation. By using reasonable structural arrangements and material selection, frequency multiplication is realized in the visible and infrared bands. Combined with Janus characteristics, signal multiplication and division operations are achieved in the forward and backward directions, respectively.

The transfer matrix method (TMM) is a powerful tool for the analysis of multilayer optical systems by decomposing the multilayer system into a series of monolayer films and using matrix operations to describe the transmission, reflection, and transmission of EWs.[23–25] However, TMM is limited to calculation, researcher is required to manually adjust the parameters in real time to observe different physical spectrum lines. Such an inefficient approach is not sustainable for future scientific advancements. In recent years, intelligent optimization algorithms have rapidly developed in the field of computing. As early as 1953, Metropolis et al.[26] presented the simulated annealing algorithm to simulate the annealing process of solid materials. By the late 1980s and early 1990s, intelligent optimization algorithms demonstrated significant advantages due to enhanced computational power, particularly in solving complex and high-dimensional optimization problems.[27] In 2017, Faris et al. introduced the Coati optimization algorithm (COA), a heuristic algorithm based on the foraging behavior of coatis to solve multi-objective optimization problems.[28] COA is inspired by the behavior of coatis, which use their flexible forelimbs and keen sense of smell to consider multiple factors (such as type, amount, accessibility, etc.) simultaneously to find the best foraging strategy. By viewing the optimization problem as the foraging process of a coati under multiple objectives (e.g., maximizing food collection,

and minimizing energy consumption), COA simulates the behavior of finding the optimal solution. The COA algorithm is employed by a series of heuristic search strategies, including scallop movement, dominance competition, and goal chasing, to achieve global optimization under multiple objectives. By simulating the foraging process of coatis, the solution space and finding better sets of solutions for multi-objective optimization problems are effectively searched by COA. Since its proposal, COA has been applied in various fields, including engineering design, machine learning, and data mining. Its unique advantage lies in its ability to consider multiple targets simultaneously and its excellent global search performance. Therefore, in this paper, the COA algorithm is used to drive TMM for calculating the proposed LHS. The physical parameters to be optimized are set as the calculation parameters of the COA algorithm, completing the optimization process of the COA algorithm. This COA-driven TMM optimization structure algorithm is referred to as the RAO-TMM algorithm.

In general, the proposed LHS, through optical Tamm states in the visible and infrared bands, combines the intrinsic absorption principle and nonlinear optical effects of LC to produce high and sharp frequency-doubling absorptivity peaks. Additionally, due to the introduction of the Janus concept, different functions are exhibited when EWs propagate in different directions within the LHS. In the sensing field, the detection of serum creatinine (C_{SC}), external pressure (P_e), and T_e, is realized in both forward and backward directions, all exhibiting high S, quality factor (Q), and figure of merit (FOM). Furthermore, the proposed LHS also facilitates frequency conversion, with the frequency doubling effect providing more possibilities for signal multiplication and division operations. It should be noted that the designed LHS is considered for purely theoretical studies, and specific experimental fabrication studies are beyond the scope of this paper. The physical properties obtained in this paper benefit from the multi-objective dynamic optimization of the physical parameters of the proposed LHS by the COA-TMM algorithm.

II. THEORETICAL DESIGN OF LHS

In Fig. 1, a schematic of the proposed LHS is shown, where two beams of EWs propagating in opposite directions are represented by green and yellow cylinders, and θ is used to represent the incident angle of the EW relative to the vertical planar structure. The constituent materials of the LHS include metallic silver (d_{Ag1}, d_{Ag2}) of different thicknesses, two analyte filling layers of different thicknesses (d_{Ana1}, d_{Ana2}), doped magnesium oxide (MgO) (d_{MgO}, $n_{MgO} = 16.49$), silicon (d_{Si}), germanium (d_{Ge}, $n_{Ge} = 4$), nonlinear layer (d_{Nol}), LC (d_{LC}) and Belgian beer (5.0% Alcohol Den Herberg Tarw) (d_{Be}, $n_{Be} = 1.343$).[29–34] The LHS is (Ag_1-(Ana_1-Ana_2)^2-Nol-Ag_2)-MgO-(Ag_1-Si-(Be-Ge)^4-LC-Nol-LC^4-Ag_2), where Ana, Nol, Be, and Ge on behalf of layer of analyte, nonlinear, Beer and Germanium, respectively. The proposed LHS exhibits distinct Janus characteristics, functioning differently when EWs propagate from different directions. In this paper, the high permittivity of the MgO layer is utilized to achieve total reflection of EWs, positioning it centrally within the LHS to insulate the forward and backward EW absorptivity. The arrangement of layers before and after the MgO layer enables control over the forward and backward propagation of the EWs, respectively.[13] Within the working band of the proposed LHS, the permittivity of Ag, LC, and Nol is represented as below.

As the excitation medium of optical Tamm state, the dielectric constant of Ag is expressed as follows:[35]

(a)

(b)
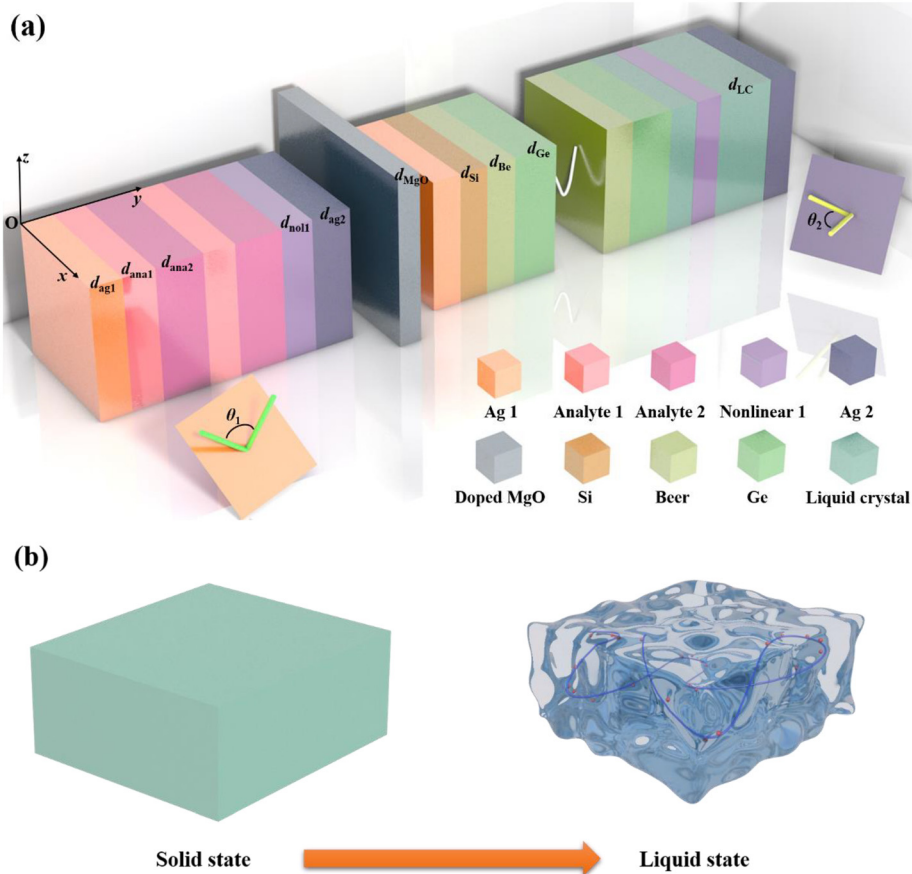
FIG. 1. (a) The model design of the proposed LHS and (b) representation of different states of LC.

$$\varepsilon_{Ag} = E_{00} - \frac{\omega_{Ag}^2}{j \cdot \omega_p \cdot r_m + \omega_p^2} - \frac{Z \cdot O_{Ag}^2}{\omega_p^2 - O_{Ag}^2 + j \cdot F_{Ag}}, \tag{1}$$

where j represents an imaginary number, $E_{00} = 2.4064$, $Z = 1.6604$ is the dielectric constant of the initial Ag layer, ω_{Ag}, O_{Ag}, F_{Ag}, and r_m are the angular frequencies $4.428\pi \times 1015$, $2.66\pi \times 1015$, $1.24\pi \times 1015$, $9.6\pi \times 1012$, respectively,[35] and ω_p is the current operating frequency.

Nonlinear media are characterized by a permittivity that varies with the applied electric field strength. Typically, the permittivity is expressed as a function, and the inverse calculation method is employed.[36] This method involves iteratively adjusting the electric field value from an initial guess until convergence is achieved, satisfying the specified condition. In this study, polystyrene was utilized as the nonlinear material.[32] The third-order nonlinear susceptibility (χ^3) is set to 1.14×10^{-12}, the ambient light intensity (It) was set to $15\,000$ lx, and the dielectric constant is expressed as follows:[37]

$$E_i = \sqrt{\frac{2 \cdot It}{c \cdot E_0}}, \tag{2}$$

where $E_0 = 8.854 \times 10^{-12}$ denotes the electric permittivity in a vacuum and $c = 3 \times 10^8$ stands for the speed of light. The expression of nonlinear RI is[37]

$$n_{Nol} = n_0 + \frac{x_3 \cdot |E|^2}{2 \cdot n_0}, \tag{3}$$

where n_0 represents the linear RI of the nonlinear material and E denotes the output electrokinetic rate of the layered structure prior to the nonlinear layer.

For the LC layer, based on the electrically controlled birefringence effect, when the LC is introduced into the LHS as a dielectric material, the effective RI of the LC can be expressed as follows:[38]

$$n_{LC} = \frac{n_o n_e}{\sqrt{n_o^2 \cos^2\theta + n_e^2 \sin^2\theta}}, \tag{4}$$

where n_o is the ordinary RI, n_e is the extraordinary RI, and θ is the angle between the direction of vertically incident light and the direction of the electric field in the electrically controlled birefringence effect.[38] In this study, E7 type LC was used. Li *et al.* determined the RIs of the E7 LC mixture at different temperatures in the infrared wavelength range using the Abbe refractometry method and wedge cell refractometry method.[33] They derived a four-parameter model to describe the temperature dependence of the LC RIs:[33]

$$n_o(T) = A - BT - \frac{(\Delta n)}{3}\left(1 - \frac{T}{T_c}\right)^\beta, \tag{5}$$

$$n_e(T) = A - BT + \frac{2(\Delta n)}{3}\left(1 - \frac{T}{T_c}\right)^\beta. \tag{6}$$

In this model, the parameter Δn represents the birefringence of the LC in its crystalline state, the exponent β is a material constant, and Tc is the critical temperature of the studied LC material.[33] Specifically, $Tc = 330$ K, $A = 1.7230$, $B = 5.24 \times 10^{-4}$, $\Delta n = 0.3485$, and $\beta = 0.2542$.[33]

EWs are incident from different directions in the front and back at angles θ_1 and θ_2, respectively, and propagate as transverse waves in the proposed LHS. In this context, while the electric and magnetic fields remain perpendicular, the electric field is parallel to the propagation direction of the incident wave, and the magnetic field is perpendicular to the propagation direction of the incident EW.[39]

To further illustrate the functionality of the LHS, the COA-TMM algorithm employed to optimize the parameters of the LHS shown in Figs. 1(a) and 1(b) represents the change of the LC state with adjustment of T_e. The forward propagation direction is represented along the plane of *yoz*. This optimization enables precise tuning of the performance of LHS, enhancing its effectiveness in various applications.

III. CALCULATION METHODS

This paper begins with Maxwell's equations, derives the traditional TMM, and presents the calculation method for the physical characteristics of EW propagation in the proposed LHS. Detailed derivations and calculations are as below.

Transverse electric waves incident vertically along the surface of the medium exhibit no electric field component in the direction of propagation perpendicular to the surface. The TMM is employed to analyze wave propagation in various media. The specific analysis is as follows: Upon incidence of light, the electromagnetic wave signal propagates from the designed LHS. Despite the absence of an electric field component in the direction of structure propagation, a perpendicular magnetic field component is present. This physical property holds true regardless of the incident direction.

Utilizing the physical conclusions derived from Maxwell's equations, equations governing the electric and magnetic fields are obtained through the iterative process, accounting for the transmission boundary conditions of both magnetic and electric fields. Subsequently, the transmission characteristics and dispersion relations of the LHS are acquired. For each single layer, the recursive matrix equation describing the relationship between the electric field and magnetic field in LHS can be expressed as follows:[40]

$$\begin{pmatrix} E_u \\ H_u \end{pmatrix} = M \begin{pmatrix} E_{u+1} \\ H_{u+1} \end{pmatrix}. \tag{7}$$

The transfer matrix in the normal dielectric layer is[41]

$$M_u^{TE} = \begin{pmatrix} \cos(k_{uz}d_u) & -\dfrac{j}{\eta_u^{TE}}\sin(k_{uz}d_u) \\ -j\eta_u^{TE}\sin(k_{uz}d_u) & \cos(k_{uz}d_u) \end{pmatrix}, \tag{8}$$

where

$$k_{uz} = k_u \cdot \cos\theta \tag{9}$$

$$k_u = \frac{\sqrt{\varepsilon_u} \cdot \omega}{c}, \tag{10}$$

$$\eta_u^{TE} = \sqrt{\frac{\varepsilon_0}{\mu_0}} \cdot \sqrt{\varepsilon_u} \cdot \cos\theta_u, \tag{11}$$

where d_u is the thickness of the uth layer and ε_u is the dielectric constant of the uth layer. According to Snell's law of refraction, where n_0 is the RI of the medium where the ray is incident, η_u is the RI of the medium where the uth layer is located, and θ_0 is the angle of incidence at which the air enters the proposed LHS.

The entire LHS comprises multiple hierarchical layers, and the connections of each layer adhere to the same transmission matrix equation. Thus, the overall structure can be expressed as follows:[40]

$$M = \sum_{j=1}^{U} M_j = \begin{pmatrix} M_{11} & M_{12} \\ M_{21} & M_{22} \end{pmatrix}. \tag{12}$$

The coefficient of reflection (r) and coefficient of transmission (t) are calculated in this way, and the equations can be expressed as follows:[40]

$$r = \frac{(M_{11} + M_{12}\eta_{U+1})\eta_0 - M_{21} - M_{22}\eta_{U+1}}{(M_{11} + M_{12}\eta_{U+1})\eta_0 + M_{21} + M_{22}\eta_{U+1}} \tag{13}$$

$$t = \frac{2\eta_0}{(M_{11} + M_{12}\eta_{U+1})\eta_0 + M_{21} + M_{22}\eta_{U+1}}. \tag{14}$$

The equations for reflectance (R), transmittance (T), and absorbance (A) are

$$R = r \cdot r^*, \tag{15}$$

$$T = t \cdot t^* \tag{16}$$

$$A = 1 - T - R, \tag{17}$$

where r^* and t^* are on behalf of the conjugate values of r and t, respectively.

Building on this foundation, the COA is utilized to drive TMM for multi-objective optimization. As a new development in 2023, COA has been compared with the results of 11 well-known metaheuristic algorithms, demonstrating its significant advantages and strong competitiveness.[41] The process of updating the position of a coati, a candidate solution in the COA, is based on modeling two natural behaviors. These behaviors include (1) strategies used by coatis when attacking iguanas and (2) the escape strategy of coati from predators.[41] Consequently, the COA population is updated in two distinct stages, reflecting these behaviors.

A. Exploration phase

Similar to other metaheuristics, the initial population of the COA is randomly generated. In the exploration phase, the COA algorithm is updated to the population position based on the foraging strategy of the coati. During this phase, the position of the coati in the search space is updated by simulating its foraging behavior. This behavior includes either climbing trees or staying on the ground to catch prey. The strategy for the search space of coati is mathematically defined to obtain the best individual position X_{max} in the current population, which is assumed to be the iguana. In the current population, it is assumed that some coatis are on a tree. Coatis on the tree update their position using the following equation:[41]

$$x_i^{o+1}(j) = x_i^o(j) + r \cdot \left(x_{best}^o(j) - I \cdot x_i^o(j)\right), i = 1, 2, \ldots, \frac{N}{2}, \tag{18}$$

where N is the population size, o is the current iteration number, r is a random number in the interval [0,1], and I represent the influence of the optimal coati, and the values are taken from the data set {1, 2}. The coati is updated by waiting for prey to be captured on the ground using Eqs. (19) and (20).[41]

$$\text{Iguana}^o_{ground}(j) = lb_j + r \cdot (ub_j - lb_j),\qquad(19)$$

$$x_i^{o+1}(j) = \begin{cases} x_i'(j) + r \cdot \left(\text{Iguana}^o_{ground}(j) - I \cdot x_i^o(j)\right), \\ \quad \text{if fitness}\left(\text{Iguana}\, a'_{ground}\right) < \text{fitness}(x_i^o), \\ x_i^o(j) + r \cdot \left(x_i^o(j) - \text{Iguana}\, a'_{ground}(j)\right), \text{else}, \end{cases}\qquad(20)$$

where Iguana^o_{ground} on behalf of the new position of the iguana after it lands on the ground. Let j denote the jth dimension variable value of the ith individual in the current iteration. In summary, individuals in the first half of the population climb the tree and Eq. (18) is used to update their position. The latter half of the population individuals wait on the ground for the iguana to land and Eqs. (19) and (20) are used to update their positions.

If the value of the objective function is improved by the new position computed for each coati, the new position is acceptable. Otherwise, the coati remains in its previous position. Essentially, one greedy selection is performed, as shown in Eq. (21).[41]

$$x_i^{t+1} = \begin{cases} x_i^{t+1}, & \text{if fitness}\left(x_i^{o+1}\right) < \text{fitness}(x_i^o), \\ x_i^o, & \text{else}. \end{cases}\qquad(21)$$

B. Development phase

In the second stage, the position of coati is updated based on its natural predator avoidance behavior. When the coati is attacked, it moves to a safer location and this phase enhances the local search capability of the COA. The escape behavior is simulated by generating a random location near the current location, as shown in Eqs. (22) and (23),[41]

$$lb_j^{local} = \frac{lb_j}{o}, \quad ub_j^{local} = \frac{ub_j}{o}, \quad o = 1, 2, \ldots, O,\qquad(22)$$

$$x_i^{o+1}(j) = x_i^o(j) - (1 - 2r) \cdot \left(lb_j^{local} + r \cdot \left(ub_j^{local} - lb_j^{local}\right)\right),\quad(23)$$

where r represents a random number between zero and one, and O is the maximum number of iterations. It can be observed that δ serves as the upper and lower bounds for updating the jth dimensional variable with each iteration. If the value of the objective function is improved by the newly computed position, the position is deemed acceptable, and Eq. (20) is used to the simulation proceeds, thereby executing one additional greedy selection. Throughout the algorithm execution, the TMM is integrated to act as the objective function, enabling the assessment of both local and global optimal values. Essentially, whenever a location is occupied by an individual coati, the TMM is invoked to calculate a numerical value, representing the magnitude of the absorptivity in the context of this study. To elucidate the execution process of the algorithm, Fig. 2 visually depicts it. The navy-blue squares denote the algorithmic process, sky blue represents the TMM execution process, while the remaining color, cobalt blue, signifies the computation process of the COA algorithm. As the COA progresses, the initialization of the data for parameters N and O is performed, and the computational dimension and scope for the TMM are determined. Following this initialization, the magnitude of the A is calculated using TMM, which serves as the position parameter X for the coati in the COA algorithm. Subsequently, Eq. (1) is utilized to update the optimization parameters, and TMM is applied to re-calculate the coati's position. Greedy selection, as described by Eq. (4), is then employed to confirm the improved coati position. Equations (2) and (3) are used to set the parameters for optimization in a manner similar to the previous step, resulting in a locally optimal coati position distinct from that in stage 1. During stage 2, Eqs. (5) and (6) are applied to further update the optimization parameters, followed by another round of greedy selection to store the obtained local optimal solutions. Finally, the local optimal solutions are compared, and the global optimal solution is selected, thereby determining the global optimal parameter combination for optimization. It should be noted that greedy selection is employed repeatedly throughout the process, primarily to enhance the identification of local optimal solutions. Greedy selection aids in finding the local optimal solution under current conditions at each step by selecting the option that maximizes the objective function value in the given state. Although greedy selection may lead to convergence on a local optimum, when combined with other exploration mechanisms (such as the randomness and diverse population update strategies used in COA), it effectively balances the relationship between exploration and exploitation, thereby mitigating the risk of becoming trapped in a local optimum.

In addition, in view of the sensing function of LHS, S, Q, and FOM should be introduced in this paper to evaluate the performance of the sensor. The specific calculation formula and used method are shown as below.

In the application of the proposed LHS for sensing, researchers have defined parameters such as S, Q, and FOM. These parameters are categorized into the frequency domain and wavelength domain, depending on the distinct calculation formulas used in different research domains. In this paper, the investigation primarily focuses on the wavelength domain. The formula is as follows:[8]

$$S = \frac{\Delta\lambda}{\Delta x},\qquad(24)$$

$$Q = \frac{\lambda_T}{FWHM},\qquad(25)$$

$$FOM = \frac{S}{FWHM},\qquad(26)$$

where λ denotes the working wavelength, Δ represents the variation in value, S signifies the relationship between the change in the detected quantity and the corresponding wavelength displacement, λ_T stands for the peak wavelength, and $FWHM$ is the wavelength difference at half of the peak.

IV. ANALYSIS AND DISCUSSION

After constructing the theoretical model, all thickness parameters in this LHS are selected as parameters to be optimized, with the optimization range constrained by the current manufacturing technology level and the size requirements of electronic devices. The objective of optimization is to identify two sharp absorptivity peaks with a multiple

16 September 2024 13:15:33
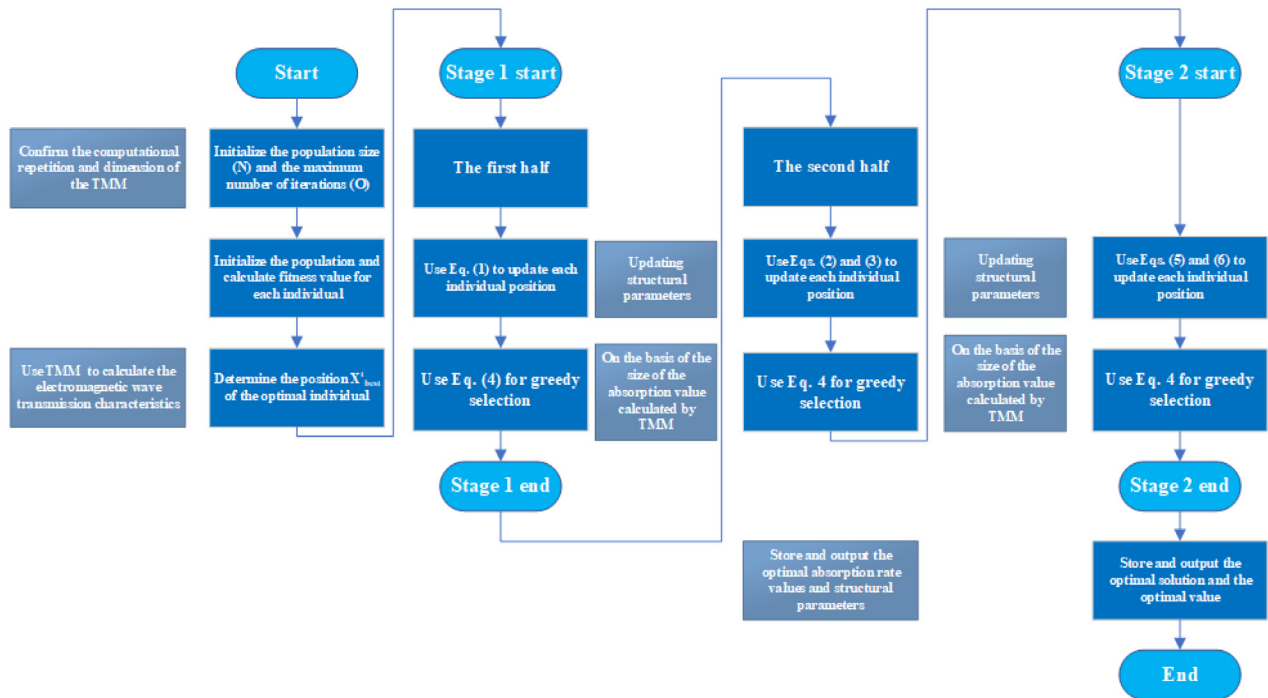
FIG. 2. The illustration of the algorithm flow of TMM-COA.

relationship close to two in the visible light and near-infrared band. The ultimate optimization outcomes are presented in Table I.

In this paper, the initial ambient T_e is set at 307 K, with the front and back EWs incident perpendicular to the LHS, and no P_e applied. The two analysis layers are filled with solutions of 85.28% creatinine concentration, and lithium niobate crystal, respectively. Leveraging the Janus property of the proposed LHS, absorptivity curves can be obtained when the EW propagates forward and backward in different directions, as illustrated in Fig. 3. The left portion of Fig. 3 illustrates that distinct sharp peak in the absorptivity curve at 774.8 and 1517.6 nm, with absorptivity exceeding 0.8, measured at 0.831 and 0.924, respectively. Notably, the curve maintains a stable working level across the entire working band, with no irregular peaks registering absorptivity greater than 0.1 within the range of 600–1800 nm. The multiple relation between 774.8 and 1517.6 nm approximates 1.96, closely resembling the doubling relationship, thereby enabling the

realization of a multiplication operation function. Consequently, when the 774.8 nm incident signal is present in the proposed LHS, a double relation signal can be outputted. This function is also achievable during backward EW propagation, as depicted in the yellow curve on the right side of Fig. 3. At 1423 and 2809 nm, the characteristic curves are exhibited absorbance rates of 0.922 and 0.991, respectively, with a multiple relation of peak wavelength measuring 1.974, indicative of a twofold division operation function. Such results play a crucial role in signal digitization.

Additionally, it is observed that the four curves with varying peak wavelengths exhibit diverse absorptivity levels and full width at half maximum (FWHM) widths, showcasing four absorptivity curves with distinct resolutions for further multifunctional sensing capabilities. This phenomenon primarily arises from that the influence of multiple physical factors on the formation of absorptivity curves. Furthermore, the study of nonlinear optical phenomena and absorptivity delved into the characteristics of Ag, with the outcomes presented in Fig. 4.

In Fig. 4(a), the absorptivity curves demonstrate the effects of removing the Ag layer and the nonlinear dielectric layer during the forward propagation of the EW, depicted in red and blue, respectively. It is evident that the Ag layer primarily induces high absorptivity peaks, as no significant absorptivity peak appears upon its removal. Conversely, when the nonlinear layer is removed, sharp absorptivity peaks still emerge at 829.2 and 1641.6 nm. However, the peak values are not as pronounced as when dielectric layers of Ag and nonlinear are present simultaneously. The multiple relationship between the different peak wavelength curves is measured as 1.974, an improvement over the original configuration. Notably, the absorptivity is enhanced

TABLE I. Optimization results of each structural parameter through COA algorithm.

Parameter	d_{ag1}	d_{ag2}	d_{ana1}	d_{ana2}	d_{MgO}
Unit	Nm	nm	nm	nm	nm
Range	$(5-10^6)$	$(5-10^6)$	$(5-10^6)$	$(5-10^6)$	$(5-10^6)$
Result	41.3	619	85	57.9	9529
Parameter	d_{nol}	d_{LC}	d_{Be}	d_{Ge}	d_{si}
Unit	nm	nm	nm	nm	nm
Range	$(5-10^6)$	$(5-10^6)$	$(5-10^6)$	$(5-10^6)$	$(5-10^6)$
Result	391	430	8.9	64	8
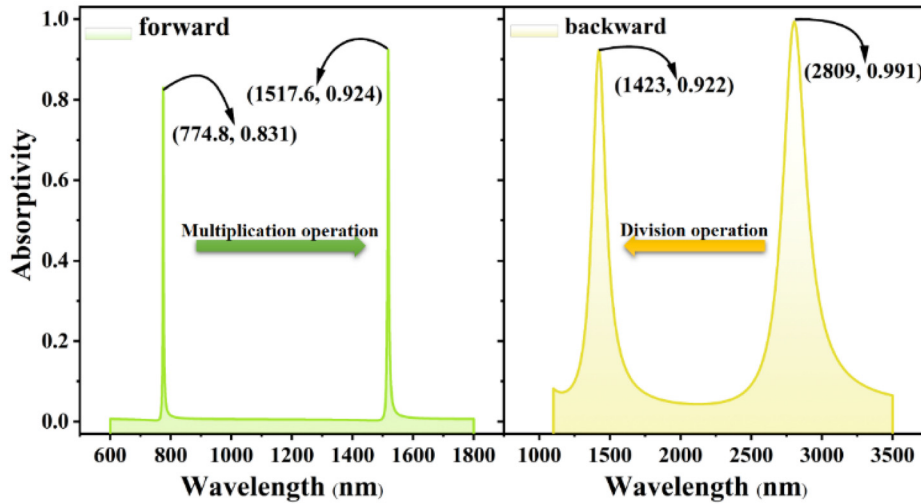
FIG. 3. Absorptivity curves for EWs transmission in different directions in the LHS.
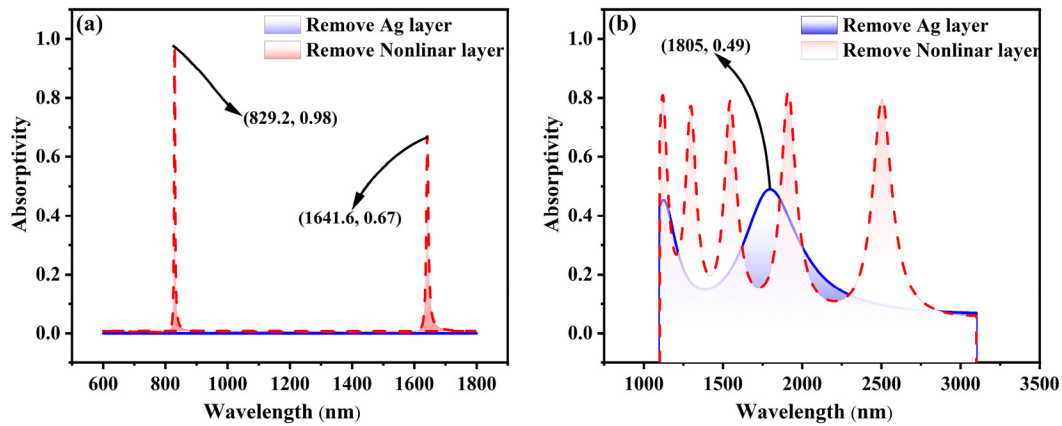
FIG. 4. Effects of Ag and Nolinar layers on absorptivity curves: (a) EWs forward and (b) EWs backward propagation.

by the addition of the nonlinear dielectric layer while impacting the doubling relationship negatively.

In Fig. 4(b), the nonlinear dielectric layer is to have a distinct role. In the backward LHS, the Ag dielectric layer continues to stimulate high numerical absorptivity peaks, while a peak is manifested solely by the nonlinear dielectric layer at 1805 nm. Its function is to concentrate scattered energy, condensing the five peaks in the original working band into two, as depicted in Fig. 3. The four generated absorptivity peaks with varying resolutions facilitate diverse sensing functions, encompassing the detection of C_{SC} and P_e during forward EW propagation, as well as the discrimination of T_e during backward EW propagation.

The detection of C_{SC} is revealed as pivotal significance in medicine as it serves as a crucial indicator for assessing renal function. The levels of C_{SC} directly mirror the filtration capacity of the kidney, aiding physicians in evaluating renal health.[42] In this study, it is observed that the sharp absorptivity peak at 774.8 nm which is exhibited a high S to changes in C_{SC} during the forward propagation of EWs. Owing to the increase in C_{SC}, significant

alterations are undergone by the equivalent dielectric constant of the solution, as depicted in Table III.[43]

A declining trend is observed in the equivalent permittivity of the solution with decreasing C_{SC}, accompanied by a noticeable red shift in the absorptivity curve, as illustrated in Fig. 5(a). The blue ellipse circles all the valid data points, and shows the specific data results in the right half of Fig. 5(a) for further processing and calculation. A negative correlation between permittivity and peak wavelength is signified by this shift, with the wavelength shifting from 774.8 to 779.2 nm, approximately linearly, while maintaining absorptivity greater than 0.8. To validate that the relationship between C_{SC} and peak wavelength is aligned with the requirements of sensing, the peak points of absorptivity curves are extracted, (774.8, 0.830), (780.8, 0.834), (786.4, 0.823), (793.6, 0.844), (797.6, 0.850), and (799.2, 0.848). Linear fitting of these points reveals a curve with a linear correlation coefficient of 0.995 and a slope of −266.67, indicating a negative correlation, as depicted in Fig. 5(b). To further evaluate the performance of sensing, S up to 266.67 μmol L^{-1}/nm is achieved using the Eq. (9). Subsequently, the numerical magnitudes of Q and FOM are determined, as illustrated in Fig. 5(c).
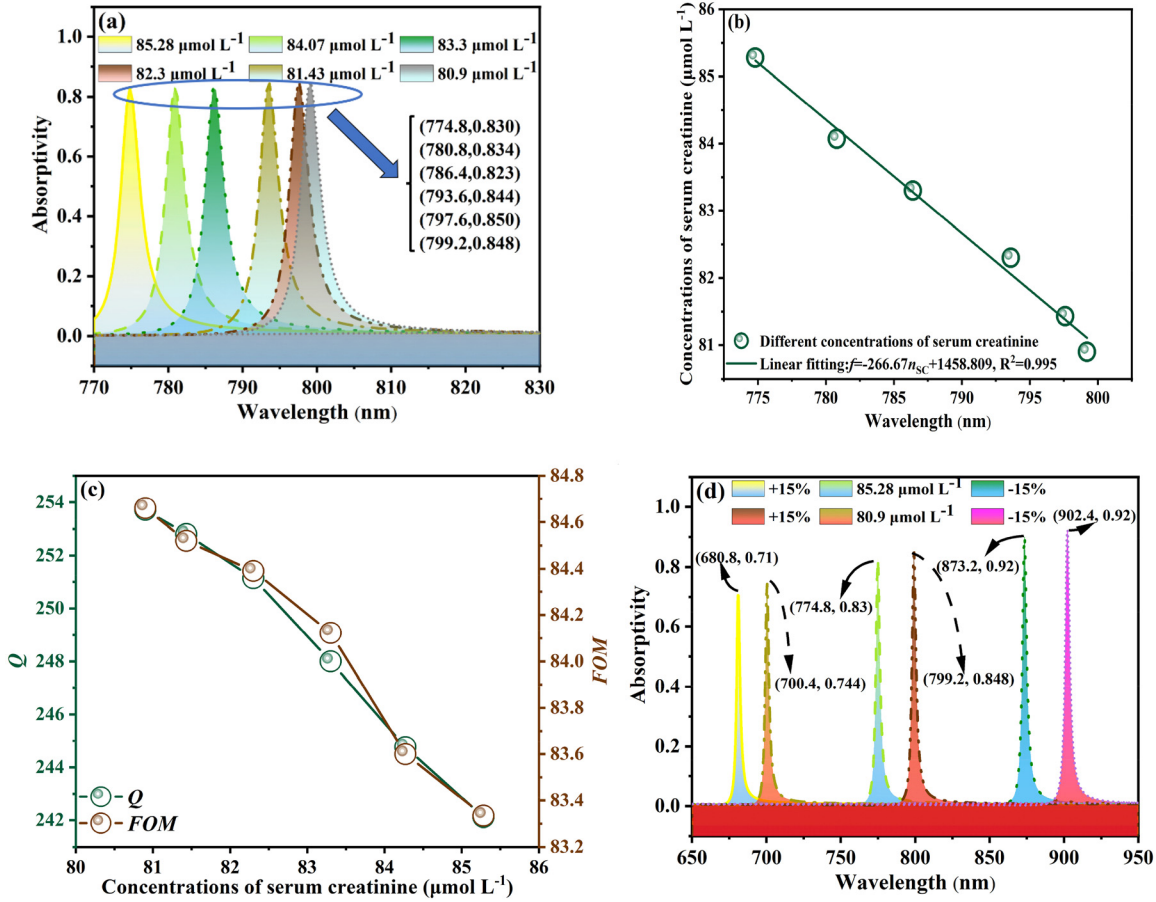
FIG. 5. (a) The absorptivity curve of the six different C_{SC} within the working wavelength band. (b) Curve relationship between working wavelength and C_{SC}. (c) Sensing properties of the sensing are characterized by evaluating the Q and *FOM*. (d) Stability analysis of sensing function of C_{SC}.

In Fig. 5(c), consistent trends are exhibited by the change patterns of Q and *FOM*, with a synchronized reduction rate. The maximum and minimum values of Q and *FOM* are 253.71 and 84.66, 242.13, and 83.33, respectively. Overall, the values tend to stabilize, indicating relatively stable performance of sensing. In Fig. 5(d), the sensing stability within the range of -15% to 15% is analyzed. When C_{SC} is doped with various water-soluble substances or subjected to artificial contamination, the proposed LHS continues to exhibit a stable absorption curve as the solution concentration varies. The changes in the maximum and minimum detectable concentrations are represented by blue and red shaded areas, respectively. By comparing the peak wavelength shifts of the absorption curves under −15%, 15%, and normal conditions across two different solution concentrations, wavelength differences of 19.6, 24.4, and 29.2 nm are observed. This gradual change in the peak wavelength difference indicates that the proposed LHS maintains stable performance in the detection of C_{SC}, which is attributed to the sensing mechanism employed in this study. The sensing is based on the variation in peak wavelength difference. Although the wavelength shift in the ideal curve can be influenced by various factors, these do not significantly impact the wavelength difference. Only the magnitude along the vertical axis A is affected, which results in a minor influence on the sensing performance, yet the sensing function remains robust.

The detection of P_e is crucial in various fields due to its role in ensuring the safe operation of systems and equipment, thereby preventing accidents and failures.[44] In industry and manufacturing, equipment failures or explosions can be averted through accurate pressure monitoring caused by overpressure or low pressure, enhancing the safety and efficiency of production processes.[44] In the medical field, pressure detection is essential for monitoring the vital signs of patients and ensuring the proper functioning of medical devices.[44]

The absorptivity peak at 1517.6 nm, as shown in Fig. 3, can be utilized for different sensing functions. The pressure-strain characteristics of lithium niobate material (LiNbO$_3$) make it suitable for this application, with the corresponding pressure S coefficient detailed in Table II.[45] Varying P_e conditions are caused by the significant changes in the dielectric constant of lithium niobate, as indicated in Table III.[46]

TABLE II. Optical coefficients of pressure-strain materials.

Material	n_0	p_{11}	p_{12}	C_1 (10^{-12}/Pa)	C_2 (10^{-12}/Pa)
LiNbO$_3$	2.29	−0.026	0.09	−2.10	2.55

16 September 2024 13:15:33

TABLE III. The equivalent permittivity values of the analyte layer filler.

P_e (GPa)	0	1	2	3	4	5
Effective permittivity	5.244	5.230	5.217	5.203	5.189	5.176
C_{SC} (μmol L^{-1})	80.9	81.43	82.3	83.3	84.07	85.28
Effective permittivity	7.081	7.049	6.964	6.812	6.073	6.579

These changes enable the detection and measurement of P_e, leveraging the S of material to ensure precise and reliable monitoring.

　　As the P_e increases from 0 to 5 GPa, the permittivity changes linearly, decreasing steadily from 5.244 to 5.176.

　　Figure 6(a) shows the absorptivity curve of the proposed LHS as it changes with P_e during the forward propagation of EWs. The overall absorptivity is remained above 0.92, with no clutter peaks in other working bands, indicating the stability of the surface sensing function. As the P_e varies from 0 to 5 GPa, the peak wavelength shifts from 1517.6 to 1511.2 nm. The data points of each peak wavelength are highlighted in Fig. 6(a). It can be found that the difference of peak wavelength between the two adjacent curves is 1.2, 1.2, 1.2, 1.1 nm,

and only the difference between the last two peaks is 0.1 nm, showing the strong linear sensing characteristics of the proposed LHS. To further analyze the relationship between P_e and peak working wavelength, the functional relationship is explored as shown in Fig. 6(b), exhibiting a negative slope and a correlation of 0.999. The $S = 213.33$ GPa/nm is calculated using Eq. (9). Figure 6(c) depicts the sensor performance. The total Q and FOM across the entire measurement range are 2089.34 and 294.34, with average values of 348.22 and 49.06, respectively. These values differ significantly from the resolution of the left absorptivity peak in Fig. 5, with the Q value being approximately 140% higher and the FOM 58% lower. Figure 6(d) employs the same analysis methodology as Fig. 5(d), with the tolerance range of -5% to 5% reflecting the standard uncertainty analysis range. Owing to the advantages of the proposed LHS, the instability range is further mitigated, and the sensing function is preserved across the broader variation range of -15% to 15%.

　　In the backward propagation of EWs, the sensing function remains operational, differing from that in the forward propagation, exhibits distinct Janus characteristics. T_e detection is crucial for preventing safety hazards such as equipment overheating, fires, or
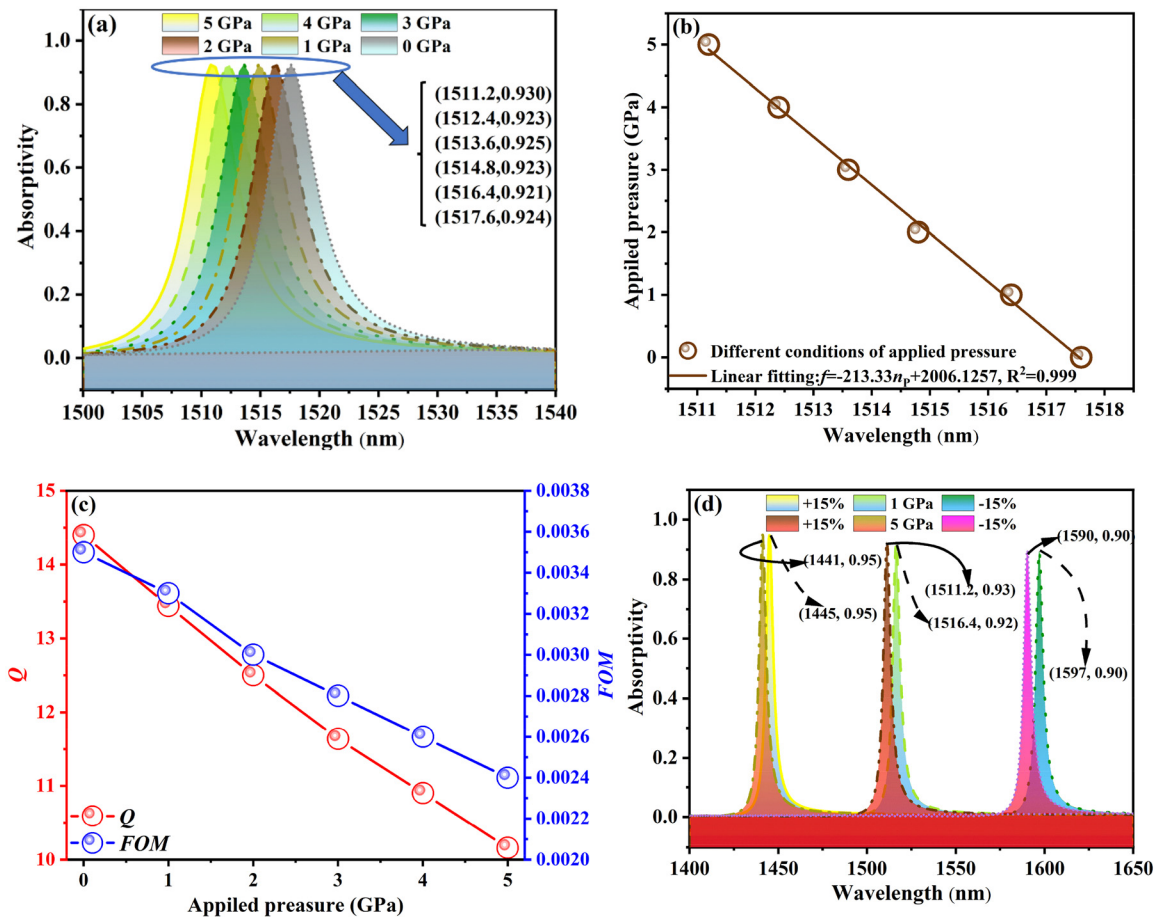
FIG. 6. (a) Influence of different P_e on the wavelength absorptivity curve of the LHS. (b) Relationship between the change of P_e and wavelength of corresponding absorptivity peak. (c) Corresponding sensing performance values Q and FOM are obtained in the different P_e. (d) Uncertainty analysis for the detection capability of P_e.
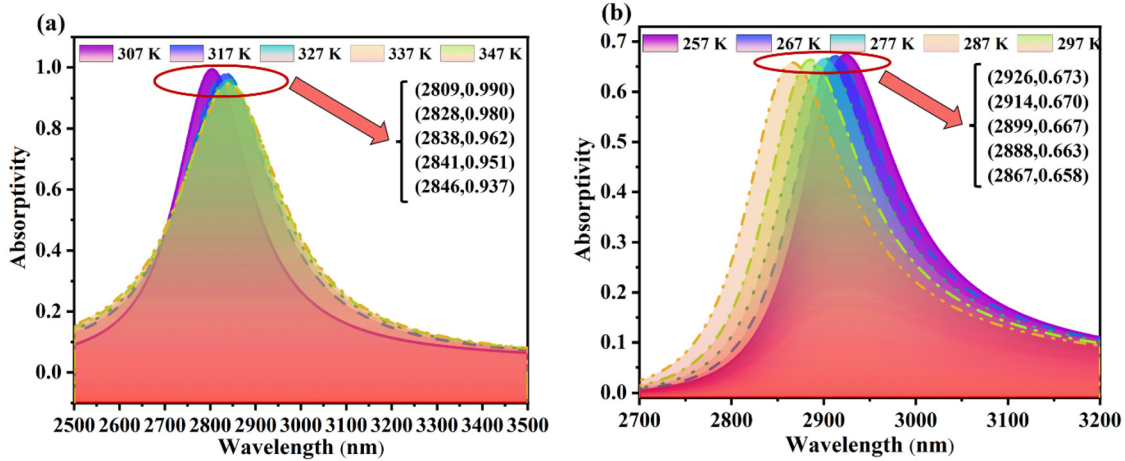
FIG. 7. When EWs is propagated back, the absorptivity curve of proposed LHS is against the change of temperature: (a) High T_e range (307–347 K) and (b) low T_e range (257–297 K).

explosions. In areas like power equipment, electronics, and automobiles, excessively high T_e can lead to catastrophic consequences, necessitating reliable T_e monitoring systems.[47] LC displays different colors within specific T_e range. As the changes of T_e, the arrangement of LC molecules alters, changing the wavelength of the reflected light and causing the LC to display different colors. The different absorptivity curves of the LHS from 257 to 347 K are measured separately by varying the T_e, as shown in Fig. 7.

From Fig. 7(a), it can be observed that measurements were taken at 10 K intervals, represented by purple, blue, cyan, flesh color, and yellow-green, respectively. The peak wavelength of the absorptivity curve shifts to the right with increasing T_e (from 307 to 347 K), a phenomenon also seen in Fig. 7(b) for the range from 257 to 297 K. Despite both T_e ranges spanning 50 K, the peak wavelength shifts are different: from 2809 to 2846 nm (37 nm difference) in Fig. 7(a), and from 2867 to 2926 nm (59 nm difference) in Fig. 7(b). This indicates that the S of the proposed LHS to T_e changes is higher in the low T_e

range (257–297 K) than in the high T_e range (307–347 K). To verify this conclusion, the peak points of the absorptivity curves are extracted. The ten data points are (257, 2926), (267, 2914), (277, 2899), (287, 2888), (297, 2867), (307, 2809), (317, 2828), (327, 2838), (337, 2841), and (347, 2846). In addition, according to the (x, y) data results obtained by the red circle in Fig. 7, it can be found that the absorption curves in both high and low temperature detection ranges maintain A good size of A, which means that the proposed LHS has a similar size of *FWHM* when dealing with the same material sensing. To some extent, it can be inferred that the proposed LHS has stable temperature sensing performance. In order to prove this conclusion, more linear analysis is needed in Fig. 8.

In Fig. 8(a), it is observed that the red and blue line fitting results represent the low and high T_e regions, respectively. In the low T_e region, the relationship between T_e and peak wavelength is positively correlated, with a S of 1.015 K/nm, significantly higher than that in the high T_e region ($S = 0.686$ K/nm), consistent with previous conclusions.
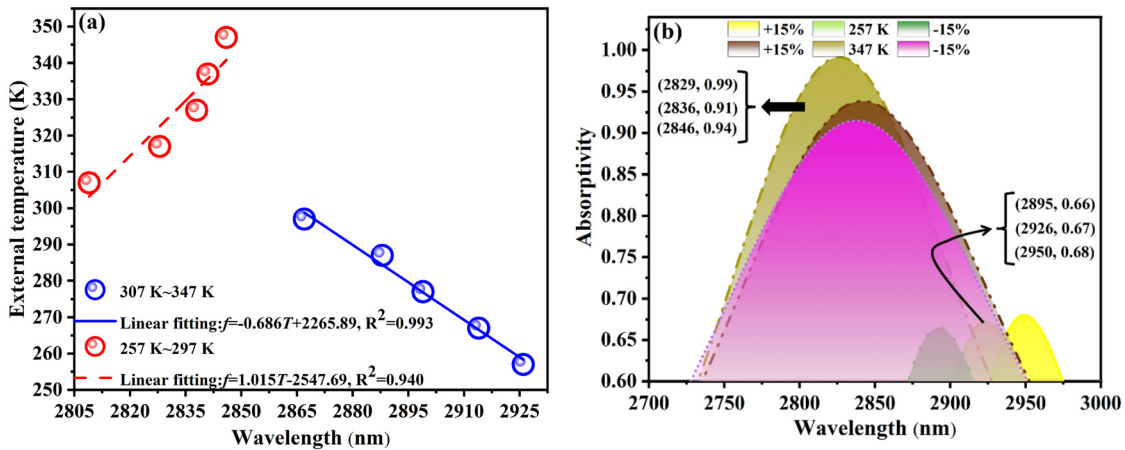
FIG. 8. (a) The curve fitting diagram of the T_e sensing function. (b) Sensing performance of T_e in parameter variations from −10% to 10%.
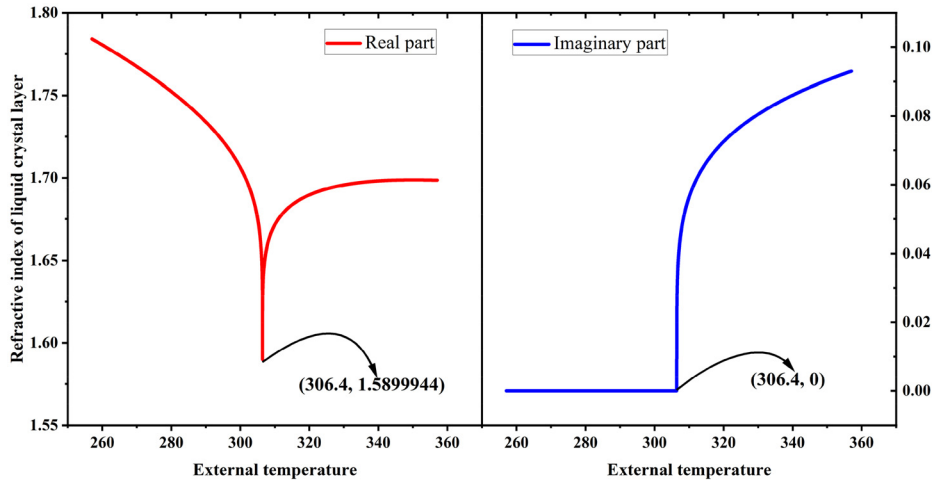
FIG. 9. The values of the imaginary and real parts of the RI at different T_e states.

The linear correlation of the two lines is 0.993 and 0.940, respectively, indicating that they can be considered linear, meeting the design requirements of the sensing function. Additionally, Fig. 8(a) reveals that the positive and negative slopes of the two curves differ, indicating a positive gradient with T_e from 257 to 297 K and a negative gradient from 307 to 347 K. In contrast to the previous analysis, the sensing performance test range in Fig. 8(b) is from −10% to 10%. This adjustment is primarily due to the unique physical characteristics of LC, which exhibit abrupt changes in material properties at specific temperatures, significantly altering the dielectric constant (as indicated by the critical temperature of 306.4 K in Fig. 9). However, this does not imply a weaker performance of the proposed structure in T_e detection. In low-temperature sensing, the proposed LHS not only maintains a stable wavelength difference but also exhibits a consistent A, indicating stable performance in low-temperature conditions. This behavior contrasts with high-temperature detection, where the RI of LC is influenced by the imaginary part within the high-temperature range, and the change in the real part follows a curve with significant curvature, which impacts the high-temperature sensing function, as illustrated in Fig. 9.

This phenomenon is mainly due to the phase behavior of LC, which exist between solid and liquid states.[38] Their molecular arrangement has a certain order, but not as completely ordered as solids. The molecular arrangement of LC changes significantly with T_e, leading to different states of matter at different T_e. To verify that the S of T_e characteristic of the proposed LHS is due to the unique physical properties of the LC, the relationship between the T_e and the RI was further explored, with results shown in Fig. 9.

In Fig. 9, the real and imaginary parts of the RI are extracted after the calculation of Eqs. (5) and (6), represented by red and blue curves, respectively. The behavior of the real and imaginary parts of the RI shows significant changes at 306.4 K. At this T_e, the real part of the RI is approximately 1.59, and its overall trend is initially decreasing and then increasing. The imaginary part of the RI begins to be numerically significant at 306.4 K. As the T_e further increases, the growth rate of the imaginary part is initially high and then low. Thus, 306.4 K is termed the critical T_e, marking the critical point of the phase change in the LC material.[33] Consequently, it can be concluded that the S of the proposed LHS is attributable to the unique physical properties of LC

materials. To further illustrate the performance of the T_e sensing function of the proposed LHS, the values of Q and FOM are calculated by Eqs. (25) and (26), as shown in Fig. 10.

In Fig. 10, hollow and solid spheres represent the high and low T_e regions, respectively, while blue and green colors denote the numerical magnitudes of Q and FOM, respectively. Over the entire range of T_e, the average values of Q and FOM in the high-T_e region are 12.576 K/nm and 0.003 04 K^{-1}, respectively, with standard deviations of 1.39 and 3.647×10^{-4}. The maximum values are 14.4 K/nm and 0.0035 K^{-1}, and the minimum values are 10.9 K/nm and 0.0026 K^{-1}. This indicates that the overall numerical changes of Q and FOM tend to be stable, reflecting relatively stable sensing performance.

In the low-T_e measurement region, the sensing performance is superior, with total Q and FOM values of 107.83 K/nm and 0.0378 K^{-1}, respectively, and average values of 21.57 K/nm and 0.0076 K^{-1}. Table IV highlights the superiority of the given LHS compared to similarly designed devices. Through comparison, it can be found that the proposed LHS has outstanding advantages in terms of calculation method, function implementation, and sensing performance.
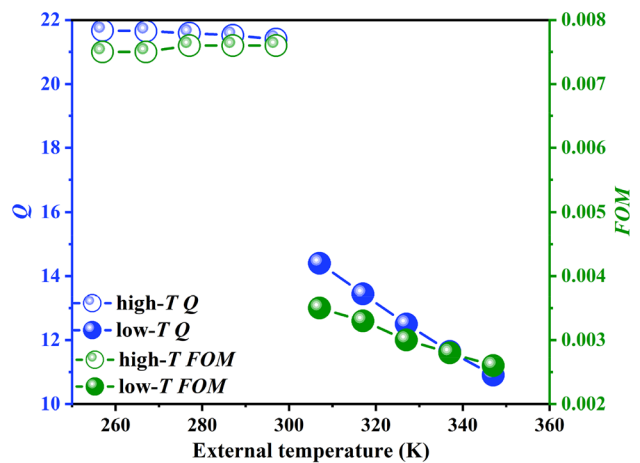
FIG. 10. The T_e sensing performance of LHS for different T_e ranges.

TABLE IV. The function of the proposed LHS compared with other published.

Reference	Calculation method	Function implementation	Janus	Sensing function	Sensing performance		
					S	Q	FOM
This work	COA-TMM	Sensing	√	C_{SC}	266.67	248.76	84.1
				P_e	213.33	348.22	49.06
		Operation		High-T_e	1.015	21.57	0.076
				Low-T_e	0.686	12.576	0.003 04
13	TMM	Sensing	√	C_{SC}	0.009 316	203.6	12.8
		Logic unit		Concentration of glucose	0.1006	1367.59	2148.07
43	TMM	Sensing	×	C_{SC}	306.25	1.03	4.8
48	Modified TMM	Sensing	×	T_e	0.010 69	None	0.0218
		Filtering					
49	Plane wave expansion	Sensing	×	P_e	17	239.53	0.2455
50	Finite difference time domain	Sensing	×	P_e	1.5	150	None
51	Finite difference time domain	Sensing	√	P_e	10	700	None
				T_e	0.67	692	None

V. CONCLUSION

In this study, a LHS combining optical Tamm states the intrinsic absorption principle of LC, and nonlinear effects are proposed. The multi-objective COA algorithm is combined with the TMM to optimize the performance of the proposed LHS, achieving an integrated device design for passive multiplication and division operations and high-performance multi-physical quantity sensing functions. The LHS exhibits Janus characteristics, displaying different physical functions depending on the direction of EW propagation. The multiple relations of 1.96 and 1.974 can be utilized in signal multiplication and division, enabling the detection of C_{SC} in forward sensing, and P_e and T_e in backward sensing. Superior performance is demonstrated by the forward sensing function, with S of 266.67 μmol L^{-1}/nm for C_{SC} and 213.33 GPa/nm for pressure. The Q and FOM for these measurements are 248.76 and 84.1 L (μmol)$^{-1}$, and 348.22 and 49.06 GPa^{-1}, respectively. The backward T_e detection is divided into high (307–347 K) and low (257–297 K) T_e regions, with performance metrics of $S = 1.015$ K/nm and 0.686 K/nm, $Q = 21.57$ and 12.576, and $FOM = 0.076$ K^{-1} and 0.003 04 K^{-1}, respectively. In future work, it is anticipated that the proposed LHS will be fabricated using chemical etching methods, followed by a series of functional tests. By integrating the experimental results with theoretical models, structural parameters will be further refined through reverse design methods. This approach aims to fully realize the sensing capabilities of the proposed LHS and facilitate its integration with various instruments, enabling its application in fields such as aerospace, environmental protection, and biosafety.

In summary, the design of this multifunctional integrated LHS provides more application possibilities for signal processing and multi-physical quantity sensing, demonstrating broad prospects and potential value.

ACKNOWLEDGMENTS

AUTHOR DECLARATIONS
Conflict of Interest

The authors have no conflicts to disclose.

Author Contributions

Jie Xu and Ming-Zhe Zhang contribute equally to this article.

Jie Xu: Formal analysis (lead); Validation (lead); Writing – original draft (lead). **Ming-Zhe Zhang:** Data curation (lead); Investigation (equal); Software (lead). **Zhao Tang:** Funding acquisition (lead); Visualization (lead); Writing – original draft (supporting). **Hai-Feng Zhang:** Conceptualization (lead); Investigation (lead); Supervision (lead); Writing – review & editing (lead).

DATA AVAILABILITY

The data that support the findings of this study are available from the corresponding author upon reasonable request.

REFERENCES

[1]B. Li and Y. Xie, "Electrical-tunable one dimensional photonic crystal laser with single liquid crystal defect layer," in *International Conference on Remote Sensing, Environment and Transportation Engineering* (IEEE, 2011), pp. 5944–5947.

[2]F. Bayat, S. Ahmadi-Kandjani, and H. Tajalli, "Designing real-time biosensors and chemical sensors based on defective 1-D photonic crystals," IEEE Photonics Technol. Lett. **28**(17), 1843–1846 (2016).

[3]M. Zheng, J. Wang, X. Zhao, T. Li, X. Liu, and L. Shi, "Arbitrary polarization conversion by the photonic band gap of the one-dimensional photonic crystal," IEEE Photonics Technol. Lett. **36**(6), 365–368 (2024).

[4]G. Calo, D. Alexandropoulos, and V. Petruzzelli, "Active photonic band-gap switch based on GaInNAs multiquantum well," IEEE Photonics J. **4**(5), 1936–1946 (2012).

[5]X. Xu *et al.*, "Advanced adaptive photonic RF filters with 80 taps based on an integrated optical micro-comb source," J. Lightwave Technol. **37**(4), 1288–1295 (2019).

[6]J. Carbonell, D. Torrent, and J. Sanchez-Dehesa, "Radial photonic crystal shells and their application as resonant and radiating elements," IEEE Trans. Antennas Propag. **61**(2), 755–767 (2013).

[7]Y. P. Yang, K. C. Lin, and I. C. Yang, "All-optical photonic-crystal encoder capable of operating at multiple wavelengths," Optik **142**, 354–359 (2017).

[8]J. Xu, C.-M. Guo, C. Yang, and H.-F. Zhang, "Theoretical study of a porous silicon cavity based on second harmonic waves formed by ferroelectric crystals for wide range multiphysical and chemical measurement," IEEE Trans. Instrum. Meas. **73**, 1–16 (2024).

[9]M. De, T. K. Gangopadhyay, and V. K. Singh, "Prospects of photonic crystal fiber as physical sensor: An overview," Sensors **19**(3), 464 (2019).

[10]J. Mathew *et al.*, "In-fiber Fabry–Perot cavity sensor for high-temperature applications," J. Lightwave Technol. **33**(12), 2419–2425 (2015).

[11]Z. A. Zaky, A. M. Ahmed, and A. H. Aly, "Remote temperature sensor based on Tamm resonance," Silicon **14**, 2765–2777 (2022).

[12]S. Khani and M. Hayati, "Optical biosensors using plasmonic and photonic crystal band-gap structures for the detection of basal cell cancer," Sci. Rep. **12**, 5246 (2022).

[13]J. Y. Sui, S. Y. Liao, and J. H. Zou, "The Janus layered metamaterial modulated by liquid crystal with multitasking of different logic gates and mode-switching biosensing," Phys. Fluids **36**(4), 047140 (2024).

[14]S. Y. Jeon, B. Shen, and N. A. Traugutt, "Synergistic energy absorption mechanisms of architected liquid crystal elastomers," Adv. Mater. **34**(14), 2200272 (2021).

[15]Q. Hao, Q. Zhang, F. Chen, K. Yang, and H. Zeng, "All-optical 20-μHz-level repetition rate stabilization of mode locking with a nonlinear amplifying loop mirror," J. Lightwave Technol. **34**(11), 2833–2837 (2016).

[16]J. Xu, Z. Tang, and J. Y. Sui, "A multimaterial sensor with Janus characteristics based on enhanced particle swarm optimization algorithm," Opt. Laser Technol. **170**, 110242 (2024).

[17]D. Marcenac and A. Mecozzi, "Switches and frequency converters based on cross-gain modulation in semiconductor optical amplifiers," IEEE Photonics Technol. Lett. **9**(6), 749–751 (1997).

[18]W. Wu and S. Tang, "Harmonic generation and impact of phase matching in multimodal multiphoton microscopy," IEEE J. Select. Top. Quantum Electron. **29**(4: Biophotonics), 1–9 (2023).

[19]K. Rivoire, S. Buckley, and J. Vučković, "Multiply resonant photonic crystal nanocavities for nonlinear frequency conversion," Opt. Express **19**(22), 22198–22207 (2011).

[20]A. Karami-Horestani, F. Paredes, and F. Martín, "Frequency-coded and programmable synchronous electromagnetic encoders based on linear strips," IEEE Sens. Lett. **6**(8), 1–4 (2022).

[21]X. Sui, Q. Wu, J. Liu, Q. Chen, and G. Gu, "A review of optical neural networks," IEEE Access **8**, 70773–70783 (2020).

[22]L. Qu, Z. Gu, and C. Li, "Bright second harmonic emission from photonic crystal vertical cavity," Adv. Funct. Mater. **33**(47), 2308484 (2023).

[23]C.-z. Li, S.-b. Liu, X.-k. Kong, H.-f. Zhang, B. r. Bian, and X.-y. Zhang, "A novel comb-like plasma photonic crystal filter in the presence of evanescent wave," IEEE Trans. Plasma Sci. **39**(10), 1969–1973 (2011).

[24]A. L. Reynolds, U. Peschel, and F. Lederer, "Coupled defects in photonic crystals," IEEE Trans. Microwave Theory Tech. **49**(10), 1860–1867 (2001).

[25]H. Sayed, Z. S. Matar, and M. Al-Dossari, "The design and optimization of an anti-reflection coating and an intermediate reflective layer to enhance tandem solar cell photons capture," Crystals **12**(1), 57 (2021).

[26]N. Metropolis, A. Rosenbluth, and M. Rosenbluth, "Simulated annealing," J. Chem. Phys. **21**(161–162), 1087–1092 (1953).

[27]A. G. Gad, "Particle swarm optimization algorithm and its applications: A systematic review," Arch. Comput. Methods Eng. **29**(5), 2531–2561 (2022).

[28]M. R. Rao and S. Sundar, "An efficient method for optimal allocation of resources in LPWAN using hybrid coati-energy valley optimization algorithm based on reinforcement learning," IEEE Access **11**, 116169–116182 (2023).

[29]H. U. Yang, J. D'Archangel, and M. L. Sundheimer, "Optical dielectric function of silver," Phys. Rev. B **91**(23), 235137 (2015).

[30]H. H. Li, "Refractive index of silicon and germanium and its wavelength and temperature derivatives," J. Phys. Chem. Ref. Data **9**(3), 561–658 (1980).

[31]F. Zhang, S. Feng, and K. Qiu, "Mechanically stretchable and tunable metamaterial absorber," Appl. Phys. Lett. **106**(9), 091907 (2015).

[32]M. A. Hosen, A. Khosravi, S. Nahavandi, and D. Creighton, "Control of polystyrene batch reactor using fuzzy logic controller," in *IEEE International Conference on Systems, Man, and Cybernetics* (IEEE, 2013), pp. 4516–4521.

[33]J. Li, S. T. Wu, S. Brugioni, R. Meucci, and S. Faetti, "Infrared refractive indices of liquid crystals," J. Appl. Phys. **97**(7), 073501 (2005).

[34]A. G. Mignani, L. Ciaccheri, and A. A. Mencaglia, "Optical measurements and pattern-recognition techniques for identifying the characteristics of beer and distinguishing Belgian beers," Sens. Actuators, B **179**, 140–149 (2013).

[35]B.-F. Wan, Q.-Y. Wang, H.-M. Peng, H.-N. Ye, and H.-F. Zhang, "A late-model optical biochemical sensor based on OTS for methane gas and glucose solution concentration detection," IEEE Sens. J. **21**(19), 21465–21472 (2021).

[36]A. Kumar, V. Kumar, B. Suthar, M. Ojha, K. S. Singh, and S. P. Ojha, "Trapping of light in nonlinear 1-D photonic crystal," IEEE Photonics Technol. Lett. **25**(3), 279–282 (2013).

[37]S. Rao, Y. Zhou, B.-F. Wan, and H.-F. Zhang, "Tunable polarization encoder capable of polarization conversion and separation based on a layered photonic structure," IEEE J. Select. Top. Quantum Electron. **29**(1: nonlinear integrated photonics), 1–8 (2022).

[38]T. H. Zhang, B. F. Wan, J. Y. Sui, and H. F. Zhang, "Angle selectivity of liquid crystal superstructure and applications in bio-detection," Phys. Fluids **36**(4), 047123 (2024).

[39]Y. Uemura, A. K. Hayashi, and M. Asahara, "Transverse wave generation mechanism in rotating detonation," Proc. Combust. Inst. **34**(2), 1981–1989 (2013).

[40]C.-T. Hung, Y.-C. Syu, T.-T. Wu, and T.-C. Lu, "Design of low-threshold photonic crystal surface-emitting lasers," IEEE Photonics Technol. Lett. **24**(10), 866–868 (2012).

[41]M. Dehghani, Z. Montazeri, and E. Trojovská, "Coati optimization algorithm: A new bio-inspired metaheuristic algorithm for solving optimization problems," Knowl.-Based Syst. **259**, 110011 (2023).

[42]G. L. Myers, W. G. Miller, and J. Coresh, "Recommendations for improving serum creatinine measurement: A report from the Laboratory Working Group of the National Kidney Disease Education Program," Clin. Chem. **52**(1), 5–18 (2006).

[43]A. H. Aly, D. Mohamed, and M. A. Mohaseb, "Biophotonic sensor for the detection of creatinine concentration in blood serum based on 1D photonic crystal," RSC Adv. **10**(53), 31765–31772 (2020).

[44]S. Sarkar, G. Ghosh, and A. Mohanta, "Arduino based foot pressure sensitive smart safety system for industrial robots," in *Second International Conference on Electrical, Computer and Communication Technologies (ICECCT)* (IEEE, 2017), pp. 1–6.

[45]M. Huang, "Stress effects on the performance of optical waveguides," Int. J. Solids Struct. **40**(7), 1615–1632 (2003).

[46]S. Zhang *et al.*, "Surface acoustic wave devices using lithium niobate on silicon carbide," IEEE Trans. Microwave Theory Tech. **68**(9), 3653–3666 (2020).

[47]C. R. Ahn, S. H. Lee, and C. Sun, "Wearable sensing technology applications in construction safety and health," J. Constr. Eng. Manage. **145**(11), 03119007 (2018).

[48]M. M. Abadla, H. A. Elsayed, and A. Mehaney, "Novel design for the temperature sensing using annular photonic crystals," Silicon **13**(12), 4737–4745 (2020).

[49]S. Dinodiya and A. Bhargava, "A comparative analysis of pressure sensing parameters for two dimensional photonic crystal sensors based on Si and GaAs," Silicon **14**(9), 4611–4618 (2021).

[50]T. Dharchana, A. Sivanantharaja, and S. Selvendran, "Design of pressure sensor using 2D photonic crystal," Adv. Natural Appl. Sci. **11**(7), 26–30 (2017).

[51]R. Rajasekar and S. Robinson, "Nano-pressure and temperature sensor based on hexagonal photonic crystal ring resonator," Plasmonics **14**, 3–15 (2018).

16 September 2024 13:15:33